Experimental Aerodynamics of a Small Fixed-Wing UAV Coated with Bio-Inspired Microfibers Under Static and Dynamic Stall

Dioser Santos , Guilherme Fernandes , Victor Maldonado *

Posted Date: 18 October 2024

doi: 10.20944/preprints202410.1381.v1

Keywords: unmanned aerial vehicle aerodynamics; bio-inspired surfaces; passive flow control

Article

Experimental Aerodynamics of a Small Fixed-Wing UAV Coated with Bio-Inspired Microfibers Under Static and Dynamic Stall

Dioser Santos †, Guilherme Fernandes † and Victor Maldonado *,†

Flow Control and Aerodynamics Lab, Department of Mechanical Engineering, Texas Tech University, Lubbock, TX 79409, USA

* Correspondence: victor.maldonado@ttu.edu

† These authors contributed equally to this work.

Abstract: A passive flow control technique in the form of microfiber coatings with diverging pillar cross-section area was applied to the wing suction surface of a small tailless unmanned aerial vehicle (UAV). The coatings are inspired from 'gecko feet' surfaces and their effect on aerodynamic and control surface performance is analyzed via wind tunnel experiments in static and dynamic conditions. The static angle of attack was set at a range of angles from -2° to 17°, and the elevon control surface was deflected from -18.7° to 24.7°. In forced oscillation, various combinations of mean angle of attack, frequency and amplitude were explored. The aerodynamic coefficients were calculated from load cell measurements for experimental variables such as microfiber pillar height, the region of the wing coated with microfibers, Reynolds number and angle of attack. Microfibers with a 140μm pillar height, when compared to the smooth wing case, provide drag reduction of up to 24.7% for C_L = 0.9 at the cruise Reynolds number, whereas shorter 70μm microfibers perform better at the stall Reynolds number, with a 24.2% CD reduction for the same CL. Control surface experiments show pitch moment authority is significantly improved at higher angles of attack near stall when microfibers cover the elevon and its upstream wing region, with an increase in CM magnitude of up to 22.4%. Dynamic experiments showed that microfibers marginally increase dynamic damping in pitch, improving load factor production in response to control surface actuation at low angles of attack, but reducing it at higher angles. In general, the microfiber pillars are within the laminar boundary layer, and create a periodic slip condition on the top surface of the pillars which increases the near-wall momentum over the wing surface. This mechanism is particularly effective in mitigating flow separation at high angles of attack, reducing pressure drag and restoring pitching moment authority provided by control surfaces.

Keywords: unmanned aerial vehicle aerodynamics; bio-inspired surfaces; passive flow control

1. Introduction

The popularization of unmanned aerial vehicles (UAV) and their success at performing a myriad of roles have resulted in exponential development and commercialization. It is estimated that the drone market will expand at a compound annual growth rate of 57.5% through 2028, with an expected revenue of 501.4 billion dollars according to [1]. This indi- cates an enormous growth potential in the field, encouraging improvement opportunities in UAV technology.

Various methods of passive flow control are regularly employed in fixed-wing aircraft to improve aerodynamic efficiency by diminishing flow separation or to correct undesirable stall behavior. Vortex generators, wing fences, notches and strakes are some flow control methods commonly employed in conventional aircraft [2,3]. In a high Reynolds number regime, the turbulent boundary layer has greater resistance to detachment, resulting in better aerodynamic characteristics [4]. In contrast, small unmanned aerial vehicles usually operate at low or transitional Reynolds numbers, where laminar separation can occur, increasing pressure drag significantly. In these situations, passive flow control techniques such as vortex generators, bumps, trips and roughness

 doi:10.20944/preprints202410.1381.v1

elements can enhance performance by causing the flow to transition earlier, therefore delaying flow separation and reducing pressure drag [5–9].

Immense technological advances in manufacturing and the miniaturization of elec- tronics have made it possible for scientists and engineers to be inspired by nature for the creation of the next generation of vehicles. Increasing focus has lately been given to bio-inspired aerodynamic and hydrodynamic structures, mostly elements found on the skin surface of aquatic mammals, fish, special feathers in birds [10] or flight mechanisms inspired from insects and bats [11–13]. Protuberances resembling the tubercles found on humpback whale flippers have been widely studied and found to increase performance and delay stall [14–16]. Fish scales' effect on wall-bounded flow behavior have been ana- lyzed experimentally and numerically, showing that small surface features can improve the aerodynamic performance of aquatic vehicles by generating vortices that reduce drag [17–20]. Similarly, micrometric structures found on shark skin called denticles (Figure 1a) have been analyzed and determined to reduce pressure drag by reducing the degree of flow separation [21–25]. In this study, similar structures in the form of microfibers inspired from gecko feet surfaces or 'setae' (Figure 1b,c) are applied to the surface of a small fixed-wing UAV and their performance is assessed through wind tunnel experiments. In previous two-dimensional studies, they have been shown to reduce flow separation by re-energizing the boundary layer through pressure modulations at the top surface of the microfibers, leading to smaller flow re-circulation areas in the separated region (Figure 1d) [26,27]. The microfibers mitigate flow separation without the disadvantage of producing higher turbulent kinetic energy, and as a result, higher viscous losses — an issue that is usually present in passive flow control methods that rely on boundary layer transition. Additionally, the microfibers used in this work have an advantage over shark skin denticles in that they are manufactured onto adhesive films that can be easily applied to any smooth surface, instead of being 3D printed. This avoids the limitations associated with additive manufacturing, such as increased time and cost to manufacture intricate structures.

The aircraft model used in this study is based on a design named Switchblade, an unmanned aerial vehicle developed under a family of reconfigurable vehicles sharing a modular framework [28–30]. The reconfigurability feature enables multiple UAV variants with the same center body structure but different mission profiles including 'low-speed high endurance' (LSHE) and 'high-speed long range' (HSLR) to be set up for flight. In this study, microfibers are applied to the UAV-HSLR variant to evaluate how its aerodynamic performance may be enhanced further.

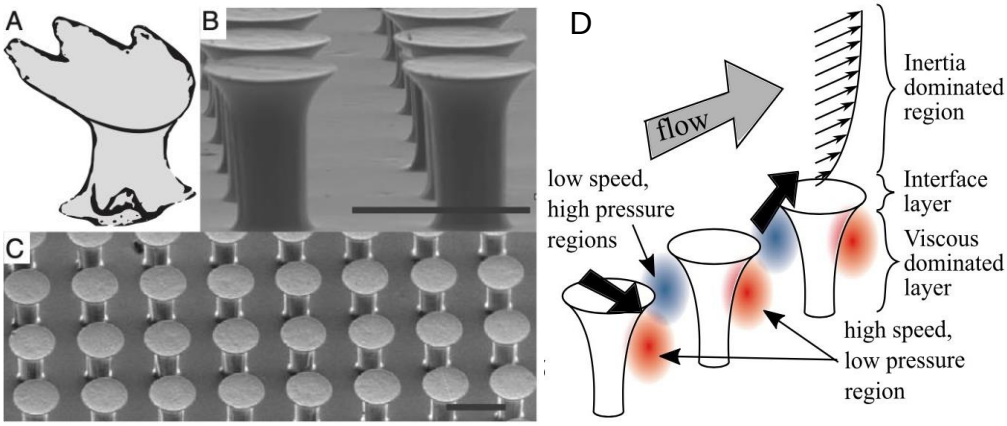

Figure 1. a) Geometry of a shark denticle, b) Side view of the bio-inspired microfibers; scale bar ≈ 100 μm, c) Top view of an array of microfibers, and d) Pressure modulations and momentum transfer along the microfiber surface. Adapted from [26].

2. Test Setup

2.1. Switchblade UAV Model

The Switchblade UAV consists of a tailless blended-wing-body that allows swapping wing modules for distinct mission performance requirements. In this work, a half-body model of the HSLR

 doi:10.20944/preprints202410.1381.v1

variant was tested in a wind tunnel. The aircraft has a low aspect ratio and wing area, with moderate leading edge sweep to attain a cruise speed of Mach 0.1. This corresponds to an airspeed of approximately 34.3 m/s near sea level conditions. The concept is illustrated in Figure 2, and some of its design variables are in Table 1. The balloons indicate regions of the wing suction surface that were covered with bio-inspired microfibers. Region 1 is upstream of the control surface (region 2), and region 3 is the remaining wing surface area up to the center body. The model was not totally covered due to the challenge of applying the adhesive film to tight corners, such as the nacelle fillets and the leading edge, although it was ensured that microfibers were located upstream of the wing's maximum thickness location.

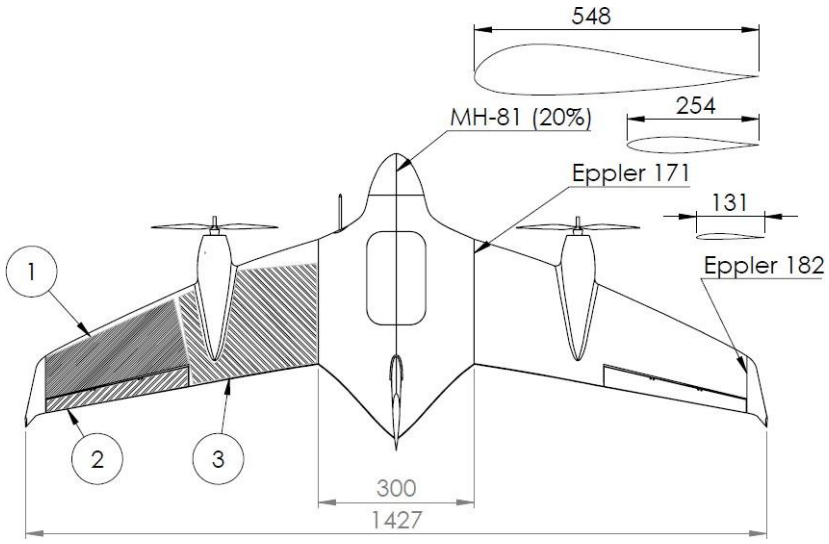

Figure 2. Top view of Switchblade small flying wing UAV (dimensions in mm.

Table 1. Wing characteristics.

Wing area [m^2]	Aspect ratio	Span [m]	LE Sweep	Taper ratio
0.324	6.3	1.43	24^o	0.35

The model structure was built almost entirely via additive manufacturing, employing a carbon-reinforced nylon material and finishing the surface with fine-grit sandpaper, to ensure that the baseline surface was free of imperfections that could affect results. Due to its reconfigurable feature, the model has the wing module attached to the center section with tubular spars, allowing for different wings to be tested as well — although this was not explored in this study. The wind tunnel model was manufactured with the same methods as a flight worthy prototype, which offers the additional possibility of evaluating its structural integrity in flight conditions for further research. The nacelle cover shown in Figure 4 may also be removed to install motor and propeller for propulsion tests, something that was accomplished in [28].

2.2. Bio-Inspired Microfiber Films

The micro-structures used in this study consist of diverging cylindrical pillars, such as described in Figure 3a. They are built with an approximate glass-shape, with a base, a diverging cylindrical pillar that increases in diameter towards the tip, where the flat face interacts with the external flow. The substrate to which the fibers are attached is an adhesive film, firmly adhered to the aircraft surface. Small fibers have a height of approximately $40\mu m$, medium fibers $70\mu m$, and tall fibers $140\mu m$. They are tightly packed on the substrate forming an array with $120\mu m$ spacing between each pillar. The base and tip diameter of each pillar is 40 μm and 75 μm respectively. This geometry and spacing allows two main flow mechanisms to develop: an internal high-speed and low pressure flow under the canopy, and a low-speed high pressure flow at the interface layer as shown in Figure 1d. An in-depth

 doi:10.20944/preprints202410.1381.v1

study of the flow physics involved with the microfibers was provided by [26,27]. These flow mechanisms are the basis for the pressure modulation effect that is transferred to the external flow. The experiment model covered with microfiber coating is shown in Figure 3. The microfibers were manufactured and provided by Setex Technologies, and were studied with respect to the effect of microfiber pillar height, referring to the height of the cylindrical micro structures on the surface shown in Figure 1. The microfiber coatings were provided in two types, with approximately $70\mu m$ and $140\mu m$ pillar heights.

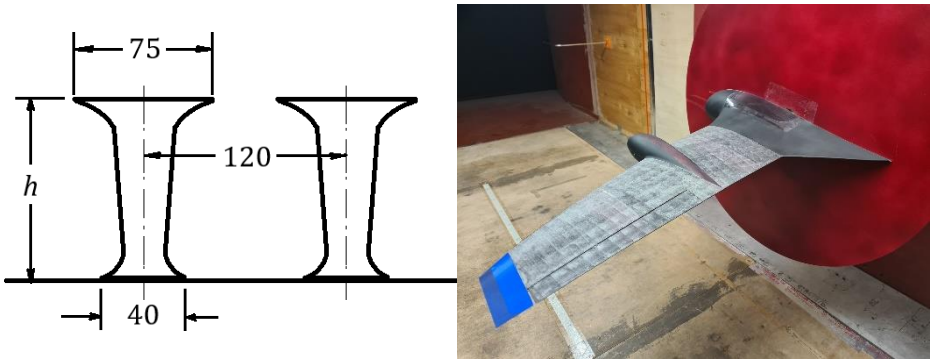

(**a**) (**b**)

Figure 3. (**a**) Microfiber schematic (dimensions in μm); (**b**) Wing covered with microfiber coating.

2.3. Wind Tunnel

The experiments were conducted in the National Wind Institute (NWI) closed-loop, subsonic wind tunnel at the Reese Technology Center. The test section is $1.2m$ tall and $1.8m$ wide, which is large enough to accommodate the aircraft half-model in its true scale, as shown in Figure 4. The half-model is attached to a circular splitter plate and connected to an ATI 9150 Net Gamma 6-DoF load sensor with a resolution of 0.025 N for the lift and drag forces and 0.00125 N-m for the pitching moment. Load cell data was acquired using a National Instruments DAQ model 6353 with a sampling rate of 1,000 Hz for a minimum of 30 seconds in each test run. The pitch attitude was set automatically with a high-torque stepper motor with an positioning resolution of 0.1°. The angle was measured throughout each experiment with a digital inclinometer, with a 0.1° resolution. To enable control surface deflection, the model was also equipped with a servo motor installed in the wing module, as in the flying prototype.

2.4. Static Angles of Attack

Microfibers were applied to different regions of the wing to identify correlations between the extent of their use and effect on aerodynamic performance. Three cases were studied: i) top of wing (all regions covered); ii) outboard, covering elevon and upstream (regions 1 and 2 only); iii) smooth wing (baseline case). For each case, two distinct free stream speeds were considered: $30m/s$ and $17.3m/s$, which correspond to the aircraft cruise speed (or very close to it) and the estimated stall speed, respectively. The different flow speeds are meant to produce distinct flow Reynolds numbers — yet consistent with the actual UAV operating and flight conditions. For nomenclature purposes, the higher speed cases are referred to as"cruise Re" and lower speed as "stall Re".

In cases not involving control surface deflection, aerodynamic forces were measured for an angle of attack range from −2° to 17°. The angle was changed manually and the model locked in position, with the wind tunnel turned off between test runs to avoid the effect of hysteresis or bias on the load cell. The control surface performance experiments were accomplished by deflecting the elevon from −18.7° to 24.7° at each of three angles of attack: 2°, 7° and 12°. Note that a negative deflection angle corresponds to a downward movement of the elevon and an increase in the sectional lift produced. The cases summary is shown in Table 2.

 doi:10.20944/preprints202410.1381.v1

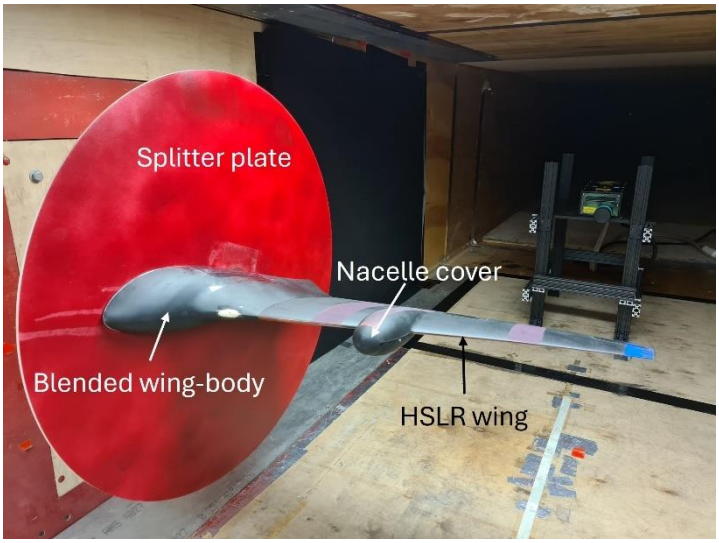

Figure 4. Wind tunnel setup with HSLR.

Table 2. Static Experiment Cases.

Surface	Region	AoA [deg]	Airspeed, U_∞	Elevon deflection, δ_e
no fibers	N/A	−2° to 17°	cruise	N/A
no fibers	N/A	−2° to 17°	stall	N/A
140μm fibers	1, 2, 3	−2° to 17°	cruise	N/A
140μm fibers	1, 2, 3	−2° to 17°	stall	N/A
140μm fibers	1, 2	−2° to 17°	cruise	N/A
140μm fibers	1, 2	−2° to 17°	stall	N/A
70μm fibers	1, 2, 3	−2° to 17°	cruise	N/A
70μm fibers	1, 2, 3	−2° to 17°	stall	N/A
no fibers	N/A	2°	cruise	−18.7° to 24.7°
no fibers	N/A	7°	cruise	−18.7° to 24.7°
no fibers	N/A	12°	cruise	−18.7° to 24.7°
140μm fibers	1, 2, 3	2°	cruise	−18.7° to 24.7°
140μm fibers	1, 2, 3	7°	cruise	−18.7° to 24.7°
140μm fibers	1, 2, 3	12°	cruise	−18.7° to 24.7°
140μm fibers	1, 2	2°	cruise	−18.7° to 24.7°
140μm fibers	1, 2	7°	cruise	−18.7° to 24.7°
140μm fibers	1, 2	12°	cruise	−18.7° to 24.7°

2.5. Dynamic Stall Program

To evaluate the effect of microfiber coatings on aircraft performance in the dynamic regime and under the effects of dynamic stall, forced oscillation tests were executed at multiple combinations of mean angle of attack, airspeed, reduced frequency, and pitch amplitude.

The reduced frequency, k for the dynamic pitch experiments is calculated according to the following expression,

$$k = \frac{\omega \bar{c}}{U_\infty} \quad (1)$$

where ω is the pitch frequency, $\bar{c}$ is the mean aerodynamic chord of the wing, and U_∞ is the airspeed corresponding to cruise or stall. For the dynamic tests, three surface conditions were evaluated: no fibers (smooth), 70μm fibers covering the whole wing (regions 1, 2 and 3), and 70μm fibers covering the outboard section of the wing (regions 1 and 2). Table 3 summarizes the types of forced-oscillation experiments.

 doi:10.20944/preprints202410.1381.v1

Table 3. Dynamic Experiment Cases: k is the reduced frequency and A is the pitch amplitude.

Surface	Region	Mean AoA [deg]	Airspeed, U_∞	k	A [deg]
no fibers	N/A	0.0, 5.0, 10.0	cruise, stall	0.022, 0.039	5.0
no fibers	N/A	0.0, 5.0, 10.0	cruise, stall	0.011, 0.020	5.0
no fibers	N/A	0.0, 5.0, 10.0	cruise, stall	0.022, 0.039	10.0
no fibers	N/A	0.0, 5.0, 10.0	cruise, stall	0.011, 0.020	10.0
70μm fibers	1, 2, 3	0.0, 5.0, 10.0	cruise, stall	0.022, 0.039	5.0
70μm fibers	1, 2, 3	0.0, 5.0, 10.0	cruise, stall	0.011, 0.020	5.0
70μm fibers	1, 2, 3	0.0, 5.0, 10.0	cruise, stall	0.022, 0.039	10.0
70μm fibers	1, 2, 3	0.0, 5.0, 10.0	cruise, stall	0.011, 0.020	10.0
70μm fibers	1, 2	0.0, 5.0, 10.0	cruise, stall	0.022, 0.039	5.0
70μm fibers	1, 2	0.0, 5.0, 10.0	cruise, stall	0.011, 0.020	5.0
70μm fibers	1, 2	0.0, 5.0, 10.0	cruise, stall	0.022, 0.039	10.0
70μm fibers	1, 2	0.0, 5.0, 10.0	cruise, stall	0.011, 0.020	10.0

During each forced oscillation run, the data was recorded through a minimum of 30 cycles, such that a one-cycle average could be calculated for the axial and normal force coefficients (C_A and C_N), and the pitching moment coefficient (C_M). These coefficients were then used to calculate the dynamic derivatives with respect to pitch rate C_{A_q}, C_{N_q} and C_{M_q}, with the single-point method described in [31] using equations (2) to (4).

$$C_{A_q} = \frac{C_{A_{(qmax)}} - C_{A_{(qmin)}}}{\frac{c_{ref}}{2V}(q_{max} - q_{min})} \quad (2)$$

$$C_{N_q} = \frac{C_{N_{(qmax)}} - C_{N_{(qmin)}}}{\frac{c_{ref}}{2V}(q_{max} - q_{min})} \quad (3)$$

$$C_{M_q} = \frac{C_{M_{(qmax)}} - C_{M_{(qmin)}}}{\frac{c_{ref}}{2V}(q_{max} - q_{min})} \quad (4)$$

where q_{max} and q_{min} are the maximum and minimum pitch rates in the cycle, respec- tively; c_{ref} is the mean aerodynamic chord, and V the airspeed. Computing the dynamic derivatives effectively condensates the forced-oscillation data, which simplifies its further analysis.

3. Results and Discussion

3.1. Static Angles of Attack

The aerodynamic forces and pitching moment were normalized with the dynamic pressure and reference wing area to obtain the lift, drag, and pitching moment coefficients. The lift coefficient as a function of angle of attack, drag polar, and lift-to-drag, L/D ratio are shown in Figure 5a, b and c, respectively. The linear portion of the C_L vs α curves do not show an appreciable difference or improvement in the lift produced using microfibers. However, there is a marked difference after α = 10° when the flow begins to separate for the baseline case near the trailing edge region of the wing. Alternatively, the flow over the wing surface with microfibers is able to maintain higher suction pressure and therefore an appreciable increase in the lift coefficient until slightly after stall. For the wing surface covered with 140μm microfibers, C_L was 3.61% higher at cruise Reynolds number and at α = 14°. For the partially covered microfiber case, C_L was 3.89% higher under the same conditions. The 70μm microfibers case on the fully covered wing led to an 3.28% increase in C_L compared to the baseline case at α = 15°.

For the stall Reynolds number cases, the increments in C_L with microfibers were smaller for both pillar heights. It is theorized that microfibers produce a periodic yet weak positive momentum transfer mechanism to the outer flow which slightly increases the mean flow velocity. Moreover, the distance that the flow passes over the microfibers prior to flow separation also affects their ability to delay flow

 doi:10.20944/preprints202410.1381.v1

separation. More distance allows the momentum transfer to build up and become effective. In this sense, passive microfibers are a weak and distributed flow control device, whereas active synthetic jets are strong but localized flow control devices which must be placed at or near the point of flow separation to become effective.

The microfibers have a stronger and more desirable effect at reducing drag, as seen in the drag polars (Figure 5b). At the cruise Reynolds number condition, the case with fully covered top wing surface attained a maximum drag reduction of 24.7% for $C_L = 0.90$ and $\alpha = 12^{\circ}$. For the partially covered wing, drag was 23.3% lower than the baseline for the same C_L. Microfibers with $70\mu m$ pillar height reduced the drag by 19.9%. In the stall Reynolds number condition, the maximum reduction in drag at $C_L = 0.9$ was 14.8% for the wing fully covered with $140\mu m$ microfibers, 14.9% for the partially covered case, and 24.2% for the $70\mu m$ microfibers fully covering the wing.

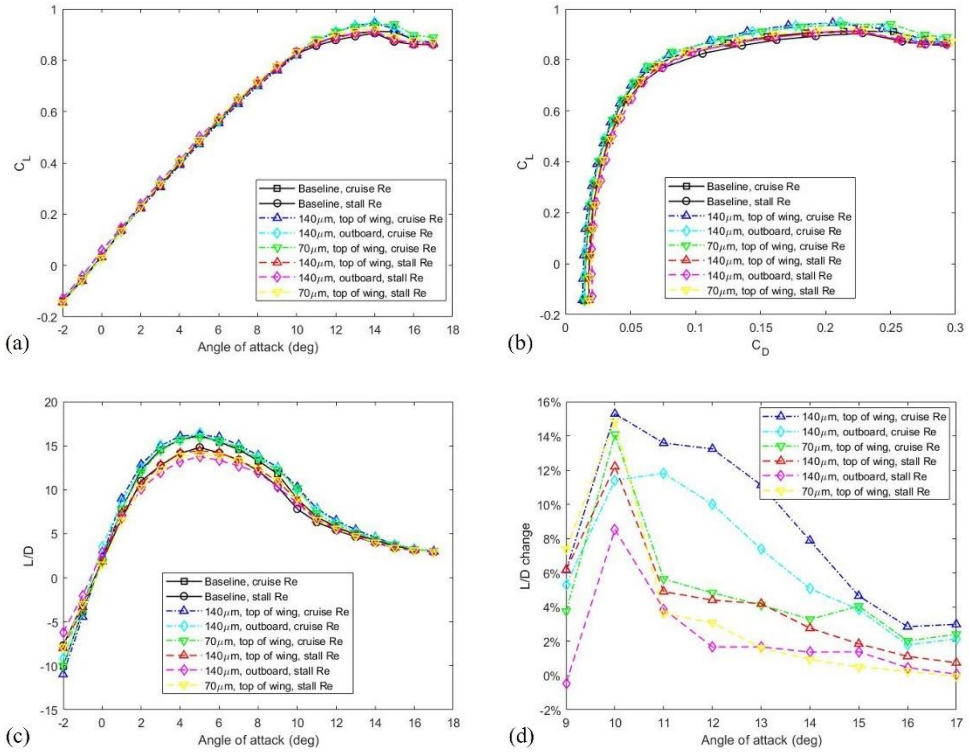

Figure 5. (**a**) Lift coefficient as a function of angle of attack; (**b**) Drag polar; (**c**) Lift-to-drag ratio, *L/D*; (**d**) High AoA L/D enhancement.

The maximum aerodynamic efficiency at cruise Reynolds number is minimally affected by the use of microfibers, where the greatest improvement in the *L/D* ratio was 1.8%, in the case with $140\mu m$ microfibers partially covering the wing (Figure 5c). In the lower *Re* regime, the use of microfibers in fact reduced the maximum *L/D* marginally. Here, the case with $140\mu m$ microfibers covering the elevon and upstream of the elevon experienced a 6.9% reduction. At higher angles of attack, all microfiber cases showed an increase in *L/D* ratio over their baselines (Figure 5d). At the cruise Reynolds number, the best performing condition is $140\mu m$ microfibers on top of the wing, with 15.3% higher *L/D* at $\alpha = 10^{\circ}$. At the stall Reynolds number, $70\mu m$ microfibers covering the top of the wing is most effective, with a 14.9% increase in *L/D* at the same angle of attack.

The results show the following trends: i) there was little difference between the cases where the entire top surface was covered and the outboard wing section only (regions 1 and 2). This indicates that in this design, microfibers are most effective at mitigating flow separation over the outboard region of the wing at high angles of attack. ii) Microfibers perform differently according to the flow regime; at higher Reynolds numbers, all cases provided similar *L/D* benefits at $\alpha = 10^{\circ}$, with $70\mu m$ fibers experiencing a sharp decline in their effect at $\alpha = 11^{\circ}$. In contrast, at lower Reynolds numbers all cases showed reduced improvement of *L/D* at $\alpha = 11^{\circ}$, followed by a further decrease at higher

 doi:10.20944/preprints202410.1381.v1

angles. Upon observation of the results for all microfiber cases at $\alpha = 10^{\circ}$, it is theorized that microfiber pillar size strongly impacts aerodynamic performance improvements at the onset of flow separation, given that the smaller microfibers provide less benefit at higher *Re*. In the more turbulent flow, the $70\mu m$ fibers do not re-energize the boundary layer in the same capacity as $140\mu m$ fibers due to the smaller secondary vortices produced and thus lower turbulent kinetic energy. Conversely, in the less turbulent flow, the highest performance enhancement is provided by the smaller fibers due to their ability to increase momentum in the outer flow without introducing excessive turbulent kinetic energy.

In order to gain more understanding about how microfibers modulate the flow in the boundary layer over an airfoil, two-dimensional particle image velocimetry (PIV) flow measurements were taken on the surface of a curved adverse pressure gradient (APG) section in turbulent flow with a LaVision PIV system. The APG section was coated throughout with microfibers containing $h = 140$ μm and subjected to a freestream velocity of 30 m/s. Two cameras with 10 cm by 10 cm measurement frames were centered about the approximate location of flow separation. Two-thousand instantaneous velocity (U, V) images were acquired and processed into time-averaged flow quantities. The mean velocity contours are presented on Figure 6.

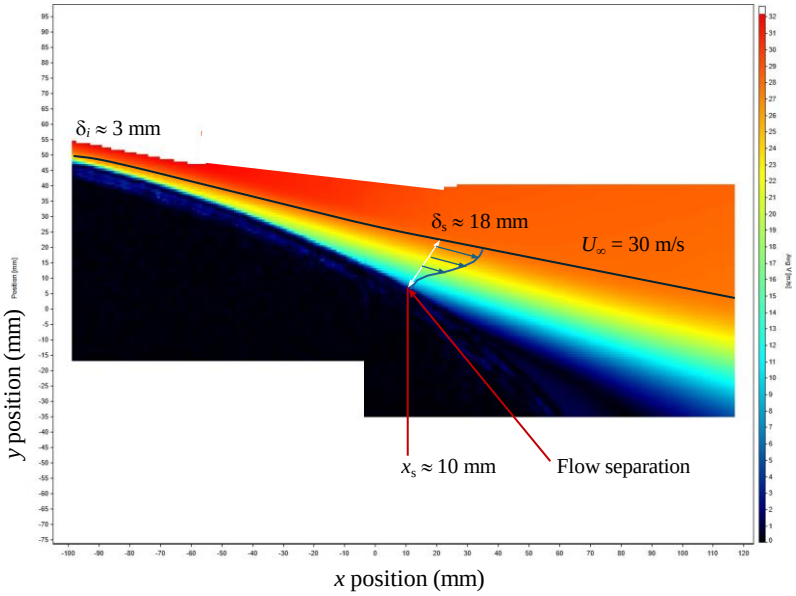

Figure 6. Time-averaged velocity over a curved APG section representative of an airfoil in turbulent flow with a freestream velocity of 30 m/s.

The turbulent boundary layer (TBL) is estimated to separate at an absolute position, $x_s \approx 10$ mm where the TBL thickness, $\delta_i \approx 18$ mm. At the inlet of the measurement domain the flow is attached and, $\delta_i \approx 3$ mm. Hence, the microfiber pillar height to boundary layer thickness, $h/\delta_i \approx 0.046$. The tip of the microfibers are within the buffer layer in the region $5 < y^+ < 30$ in terms of viscous wall units. Further upstream where the APG strength progressively decreases until the pressure gradient becomes zero, the boundary layer thickness was measured as approximately 1.3 mm. At this point, $h/\delta \approx 0.108$ where the microfibers modulate the flow within the log layer, where $30 < y^+ < 0.15\delta$ [32].

It is theorized by the authors that the microfibers are most effective when the pillar height scales with this layer given by the law of the wall,

$$u^+ = \frac{1}{\kappa} log(y^+) + B \quad (5)$$

The von Kármán constant, κ and intercept, B was found to be $\kappa = 0.384$ and $B = 4.17$ according to Österlund et al. [33]. The log layer is characterized by not only laminar shear, but also turbulent shear produced by naturally occuring velocity

 doi:10.20944/preprints202410.1381.v1

fluctuations. The micropillars mainly serve to intensify wall-normal velocity fluctuations creating alternate low-speed high pressure and high speed low pressure regions as the flow travels throughout the micropillars. The net effect is a positive momentum transfer into the outer turbulent layer ($y^+ > 0.15\delta$) which is used to overcome the external adverse pressure gradient and delay flow separation.

The control surface performance shown in Figure 7 indicates that changes in pitching moment by the use of microfibers on the surface depends on the angle of attack of the aircraft, and at certain conditions the fibers have a detrimental effect. At $\alpha = 2^\circ$, microfibers covering the top surface of the wing reduced the C_M magnitude by 11.1% for an elevon deflection angle, $\delta_e = -15^\circ$. At a moderate angle of attack of $\alpha = 7^\circ$, the microfibers showed negligible effect on control surface pitching performance. Finally, for $\alpha = 12^\circ$, the use of microfibers revealed to be very effective for elevon performance, with a maximum increase in C_M magnitude of 15.6% for $\delta_e = -15^\circ$ with the suction surface fully coated with microfibers.

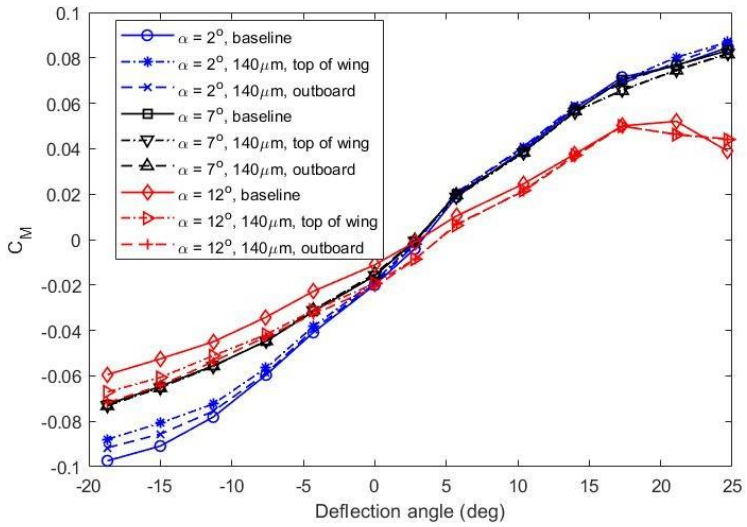

Figure 7. Elevon deflection performance: pitching moment coefficient, C_M as a function of elevon deflection angle, δ_e for the baseline and micropillar cases.

Alternatively for the partially coated wing, the increase in C_M was 22.4% at the same elevon deflection angle. This behaviour displays some nonlinear spanwise interaction on the flow between regions of microfibers, where covering the surface of the wing with additional microfiber becomes detrimental or less efficient. A similar effect was observed on a rotor with synthetic jets at transitional Reynolds numbers [34]. The most efficient use of synthetic jets in terms of improving the figure of merit of the rotor occurred in the blade tip region. Activating additional synthetic jets towards the middle and root regions of the blade showed a diminishing return in rotor thrust when considering the additional energy input to the jets. The clear similarity between the fixed-wing in this study and the referenced rotor blade is that the flow is considerably three-dimensional (3D) with spanwise flow on the wing and blade tip region. These results show that microfibers can be utilized as an effective passive flow control technique for finite wings with 3D flow and at higher angles of attack where it becomes more critical to avoid stall and thus a loss in flight control.

3.2. Dynamic Stall

Each dynamic angle of attack run from forced oscillations in pitch was generated for a one-cycle average with reduced frequency, $k = 0.039$ as shown in Figure 8. Given the high volume of data, it would be inconvenient to display the plots for all cases in a single figure, therefore the coefficients across all cases were used to calculate the dynamic derivatives, shown in Figure 9. As expected from the static test results, the strongest effect by the fibers is observed at the highest angle of attack, $\alpha = 10^\circ$. A hysteresis is defined in this study by the absolute value difference between the force or moment

 doi:10.20944/preprints202410.1381.v1

coefficient produced during dynamic pitch relative to static pitch at a given angle of attack. At α = 10°, in the dynamic axial force coefficient (C_A), the existence of microfibers seemed to marginally reduce the hysteresis effect. For the normal force coefficient, the hysteresis on the top side of the loop was moderately increased in the case with microfibers covering the entire wing, as seen in C_N (Figure 9b) and C_M (Figure 9c). This indicates a minor effect between the 70μm microfibers and the dynamic damping of the aircraft.

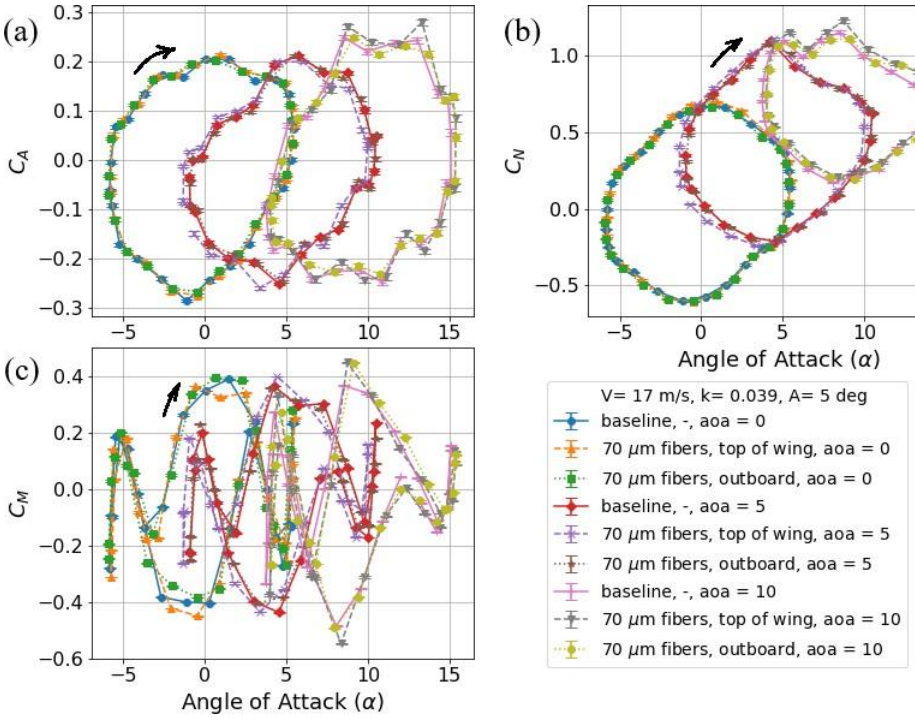

Figure 8. Dynamic pitch coefficients for different surface cases and wing coverage: (**a**) C_A; (**b**) C_N; (**c**). C_M. The black arrow indicates the direction of the pitch up maneuver.

The combined pitch derivatives are shown in Figure 9a to c. The derivatives lie in two groupings: lower speed (17 m/s) and higher speed (30 m/s), which shows a small dependence on airspeed in the results. C_{A_q} is higher at 17 m/s (Figure 9a), whereas C_{N_q} is higher at 30 m/s (Figure 9b). No particular trend is seen on C_{M_q} in respect to airspeed (Figure 9c). The effect of mean angle of attack on the dynamic behavior is small, as all cases show similar dispersion with increasing angle of attack. The normal force derivative C_{N_q} decreases modestly with increasing angle of attack as seen in Figure 9b, although not enough to suggest intensification of stability nonlinearities characteristic of high-α flight.

Preprints.org (www.preprints.org) | NOT PEER-REVIEWED | Posted: 18 October 2024 doi:10.20944/preprints202410.1381.v1

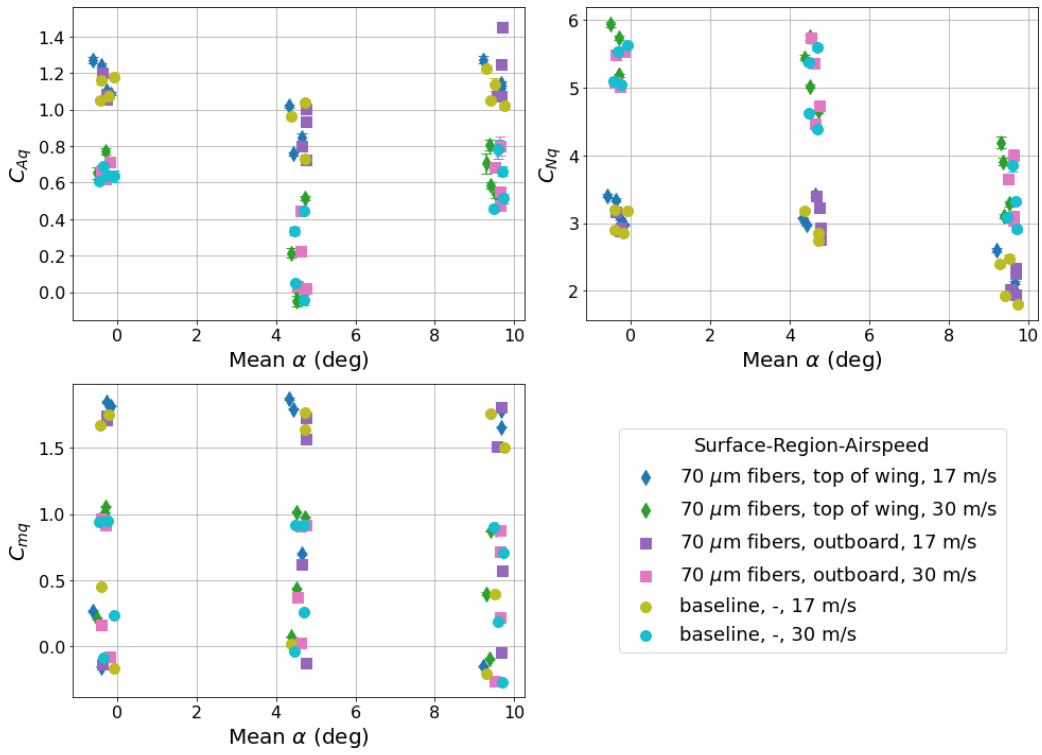

Figure 9. Dynamic derivatives in pitch: C_{Aq}; C_{Nq}; C_{mq} as a function of mean angle of attack.

Considering that the dynamic derivatives on their own do not provide a good physical sense of the aircraft's performance, a simple exercise was performed to evaluate a steady pull-up maneuver. Equation 6, found in [35], was used to estimate the load factor variation δn with respect to a unit elevon deflection $\delta\eta$.

$$\left(\frac{\delta n}{\delta \eta}\right)_{\text{steady state}} = -\frac{m_\eta z_w U_e}{m_q z_w - m_w U_e} \tag{6}$$

In this equation, m_η, m_q and m_w are the derivatives of pitching moment with respect to elevon angle, pitch rate and vertical speed, respectively. z_w is the derivative of vertical force with respect to vertical speed, and U_e the equilibrium longitudinal speed. All the derivatives are in concise form, and defined in the body coordinate system. Although C_{A_q}, C_{N_q} and C_{M_q} are not in the equation, they are implicit in the definition of m_η, m_q and m_w through the aircraft's equation of state. Equation 6 was solved for a steady-pull up maneuver at cruise speed ($30m/s$) and pitch angles of 0, 5, and 10°. These flight conditions were chosen to match the data obtained from the forced oscillation tests since the derivatives are calculated about specific mean angles of attack. Additionally, Figure 9 shows that the maximum difference between the baseline (smooth) and microfiber cases happens at the highest angle of attack. Table 4 shows the results for Equation 6.

The results show that the marginal increase in dynamic damping seen in Figure 8, by use of microfibers, has an effect on the aircraft's maneuverability. Covering the top of the wing or just the outboard region with $70\mu m\, fibers$ increased the aircraft's response to a unit elevon input at the lowest angle of attack. From $-0.14g/deg$ of elevon deflection, the load factor went up to $-0.21g/deg$ at $\alpha = 0°$. To better understand the significance of these performance metrics, consider that the Lockheed F-104A Starfighter, an interceptor aircraft, generates a response of $-0.94g/deg$ during a comparable maneuver [35]. For the tailless UAV, although less maneuverable due to the short momentum arm between control surface and center of gravity, an improvement of $0.07g/deg$ is considerable for a small change in surface treatment. For 5° or 10° angle of attack, the microfibers had lower impact on load factor response, with a decrease being observed at 10°. The pressure modulation created by the microfibers

 doi:10.20944/preprints202410.1381.v1

re-energizes the external flow under adverse pressure gradients, reducing flow separation, though it causes the aircraft to exhibit a slower response in symmetrical maneuvers at high angles of attack.

Table 4. Load factor increment per unit elevon input [g's/deg].

Case	Mean AoA	Load Factor Increment, Δn
Baseline	0.0	-0.14
$70\mu m$, top of wing	0.0	-0.17
$70\mu m$, outboard	0.0	-0.21
Baseline	5.0	-0.10
$70\mu m$, top of wing	5.0	-0.08
$70\mu m$, outboard	5.0	-0.10
Baseline	10.0	-0.04
$70\mu m$, top of wing	10.0	-0.03
$70\mu m$, outboard	10.0	-0.02

4. Conclusions

In this work, bio-inspired microfibers were applied to the top suction surface of a small fixed-wing UAV, and their effect on aerodynamic performance was studied with wind tunnel experiments. Dependence on flow regime *Re*, angle of attack, region of coverage, and microfiber pillar height was assessed for the lift and drag coefficients, as well as the *L*/*D* ratio. For a cruise Reynolds number of 3.7×10^5 with $140\mu m$ microfibers provided the greatest reduction in drag, 24.7% when covering the entire upper surface of the wing. The significance of drag reduction at high angles of attack for a flying UAV is higher climb rates and/or energy savings that increase the range of the aircraft. At the stall Reynolds number of 2.1×10^5 with $70\mu m$ microfibers, performance is maintained with a drag reduction of up to 24.2%. It was observed that improvements in performance by the use of microfibers are obtained at higher angles of attack, when flow separation is prevalent, and where the microfibers are able to delay flow separation and restore aerodynamic performance. In this manner, microfibers are functionally similar to other forms of passive flow control devices, yet are not detrimental to cruise performance. At lower angles of attack, such as $\alpha = 5^\circ$, the microfibers only had marginal effect on aerodynamic efficiency; at cruise Reynolds, *L*/*D* was increased by 1.8%, and at stall Reynolds it was reduced by 6.9%. It is believed that a positive increase in *L*/*D* can be achieved by more careful microfiber design including tuning of the microfiber pillar height so that it remains within the log-layer of the boundary layer for the tested stall and cruise Reynolds number.

The control surface with microfiber experiments yielded increased pitching moment authority for the HSLR variant at $\alpha = 12^\circ$, enhancing C_M by 22.4% with an elevon deflection of -15°. Microfibers for the first time were tested under dynamic stall conditions on a pitching wing. Under a mild stall at $\alpha = 10^\circ$, microfibers indicated a marginal reduction in the hysteresis of the dynamic axial force coefficient, while an increase in hysteresis for the normal force coefficient was shown. This indicates a decrease and an increase in the primary force components that make up drag and lift respectively which serve to increase the dynamic lift-to-drag ratio with microfibers compared to the baseline case. The small increase in dynamic damping also yielded unexpected consequences to the slower pitching moment response of the UAV model to an elevon input. The overall results show that there is proven potential in applying bio-inspired microfibers with diverging pillar cross-section area as presented in this study, to the design of small-scale fixed-wing UAVs. In particular, they can be beneficial for flight at higher angles of attack, or so called high-α flight, which is associated to a highly maneuverable UAV with superior pitch and roll performance akin to unmanned combat aerial vehicles.

Author Contributions: Conceptualization, D.S. and V.M.; methodology, D.S.; software, D.S.; validation, D.S., G.F.; formal analysis, G.F. and D.S.; investigation, G.F.; resources, D.S.; data curation, G.F.; writing—original draft preparation, D.S., G.F., and V.M.; writing—review and editing, V.M.; visualization, D.S.; supervision, V.M.; project administration, V.M. and D.S.; funding acquisition, V.M. The authors have contributed equally to all sections and tasks. All authors have read and agreed to the published version of the manuscript.

 doi:10.20944/preprints202410.1381.v1

Funding: This work was supported by the Department of Mechanical Engineering, Texas Tech University, as part of the startup package of Victor Maldonado.

Data Availability Statement: Data will be provided upon request.

Acknowledgments: The authors would like to acknowledge David Myers for his indispensable experience and help in manufacturing the experimental setup used in this work. Without him, most of the experiments would not have been possible.

Conflicts of Interest: The authors declare no conflict of interest.

Abbreviations

The following abbreviations are used in this manuscript:

UAV	Unmanned Aerial Vehicle
UAS	Unmanned Aerial System
HSLR	High-Speed Long-Range
LSHE	Low-Speed High-Endurance
AoA	Angle-of-Attack

References

1. GrandView. Commercial Drone Market Size, Share and Trends Analysis Report By Product (Fixed-wing, Rotary Blade, Hybrid), By Application, By End-use, By Region, And Segment Forecasts, 2021 - 2028.
2. Raymer, D., Aircraft Design: A Conceptual Approach; American Institute of Aeronautics and Astronautics: Reston, VA, 2012; pp. 223 – 225. https://doi.org/10.2514/4.869112.
3. Lin, J.C. Review of research on low-profile vortex generators to control boundary-layer separation. *Progress in Aerospace Sciences* **2002**, *38*, 389–420. https://doi.org/https://doi.org/10.1016/S0376-0421(02)00010-6.
4. Lissaman, P. Low-Reynolds-number airfoils. *Annual review of fluid mechanics* **1983**, *15*, 223–239.
5. Zhen, T.K.; Zubair, M.; Ahmad, K.A. Experimental and Numerical Investigation of the Effects of Passive Vortex Generators on Aludra UAV Performance. *Chinese Journal of Aeronautics* **2011**, *24*, 577–583. https://doi.org/https://doi.org/10.1016/S1000-9361 (11)60067-8.
6. Zhu, C.; Chen, J.; Wu, J.; Wang, T. Dynamic stall control of the wind turbine airfoil via single-row and double-row passive vortex generators. *Energy* **2019**, *189*, 116272. https://doi.org/https://doi.org/10.1016/j.energy.2019.116272.
7. Zhou, Y.; Wang, Z.J. Effects of Surface Roughness on Separated and Transitional Flows over a Wing. *AIAA Journal* **2012**, *50*, 593–609, [https://doi.org/10.2514/1.J051237]. https://doi.org/10.2514/1.J051237.
8. Ben-Gida, H.; Stefanini, J.; Stalnov, O.; Gurka, R. Application of passive flow control techniques to attenuate the unsteady near wake of airborne turrets in subsonic flow. *Aerospace Science and Technology* **2021**, *119*, 107129. https://doi.org/https://doi.org/10.1016/j.ast.2021.107129.
9. Serdar GENÇ, M.; KOCA, K.; AÇIKEL, H.H. Investigation of pre-stall flow control on wind turbine blade airfoil using roughness element. *Energy* **2019**, *176*, 320–334. https://doi.org/https://doi.org/10.1016/j.energy.2019.03.179.
10. Winzen, A.; Klaas, M.; Schröder, W. High-Speed Particle Image Velocimetry and Force Measurements of Bio-Inspired Surfaces. *Journal of Aircraft* **2015**, *52*, 471–485, [https://doi.org/10.2514/1.C032742]. https://doi.org/10.2514/1.C032742.
11. Hu, H.; Tamai, M. Bioinspired Corrugated Airfoil at Low Reynolds Numbers. *Journal of Aircraft* **2008**, *45*, 2068–2077, [https://doi.org/10.2514/1.37173]. https://doi.org/10.2514/1.37173.
12. Bie, D.; Li, D.; Xiang, J.; Li, H.; Kan, Z.; Sun, Y. Design, aerodynamic analysis and test flight of a bat-inspired tailless flapping wing unmanned aerial vehicle. *Aerospace Science and Technology* **2021**, *112*, 106557. https://doi.org/https://doi.org/10.1016/j.ast. 2021.106557.
13. Sui, T.; Zou, T.; Riskin, D. Optimum Design of a Novel Bio-Inspired Bat Robot. *IEEE Robotics and Automation Letters* **2022**, *7*, 3419–3426. https://doi.org/10.1109/LRA.2022.3146536.
14. Fish, F.E., Biomimetics and the Application of the Leading-Edge Tubercles of the Humpback Whale Flipper. In *Flow Control Through Bio-inspired Leading-Edge Tubercles: Morphology, Aerodynamics, Hydrodynamics and Applications*; New, D.T.H.; Ng, B.F., Eds.; Springer International Publishing: Cham, 2020; pp. 1–39. https://doi.org/10.1007/978-3-030-23792-9_1.

15. Guerreiro, J.L.E.; Sousa, J.M.M. Low-Reynolds-Number Effects in Passive Stall Control Using Sinusoidal Leading Edges. *AIAA Journal* **2012**, *50*, 461–469, [https://doi.org/10.2514/1.J051235]. https://doi.org/10.2514/1.J051235.
16. Rose, B.; Vt, G. Aerodynamics with state-of-the-art bioinspired technology: Tubercles of humpback whale. *Proceedings of the Institution of Mechanical Engineers Part G Journal of Aerospace Engineering* **2021**, *235*. https://doi.org/10.1177/09544100211001501.
17. Dou, Z.; Wang, J.; Chen, D. Bionic research on fish scales for drag reduction. *Journal of Bionic Engineering* **2012**, *9*, 457–464.
18. Chen, D.; Chen, H.; Cui, X. Dual-coupling drag reduction inspired by tuna skin: Fan-shaped imbricated fish scale composited with flexible coating. *AIP Advances* **2022**, *12*, 035218, [https://doi.org/10.1063/5.0066195]. https://doi.org/10.1063/5.0066195.
19. Mosghani, M.M.; Alidoostan, M.A.; Binesh, A. Numerical analysis of drag reduction of fish scales inspired Ctenoid-shape microstructured surfaces. *Chemical Engineering Communications* **2021**, *0*, 1–16, [https://doi.org/10.1080/00986445.2021.1992398]. https://doi.org/10.1080/00986445.2021.1992398.
20. Muthuramalingam, M.; Puckert, D.K.; Rist, U.; Bruecker, C. Transition delay using biomimetic fish scale arrays. *Scientific Reports* **2020**, *10*, 14534. https://doi.org/10.1038/s41598-020-71434-8.
21. Bixler, G.D.; Bhushan, B. Fluid Drag Reduction with Shark-Skin Riblet Inspired Microstructured Surfaces. *Advanced Functional Materials* **2013**, *23*, 4507–4528, [https://onlinelibrary.wiley.com/doi/pdf/10.1002/adfm.201203683]. https://doi.org/https://doi.org/10.1002/adfm.201203683.
22. Friedmann, E.; Portl, J.; Richter, T., A Study of Shark Skin and Its Drag Reducing Mechanism. In *Advances in Mathematical Fluid Mechanics: Dedicated to Giovanni Paolo Galdi on the Occasion of his 60th Birthday*; Rannacher, R.; Sequeira, A., Eds.; Springer Berlin Heidelberg: Berlin, Heidelberg, 2010; pp. 271–285. https://doi.org/10.1007/978-3-642-04068-9_16.
23. Domel, A.G.; Domel, G.; Weaver, J.C.; Saadat, M.; Bertoldi, K.; Lauder, G.V. Hydrodynamic properties of biomimetic shark skin: effect of denticle size and swimming speed. *Bioinspiration & Biomimetics* **2018**, *13*, 056014. https://doi.org/10.1088/1748-3190/ aad418.
24. Afroz, F.; Lang, A.; Habegger, M.L.; Motta, P.; Hueter, R. Experimental study of laminar and turbulent boundary layer separation control of shark skin. *Bioinspiration & Biomimetics* **2016**, *12*, 016009. https://doi.org/10.1088/1748-3190/12/1/016009.
25. Yu, C.; Liu, M.; Zhang, C.; Yan, H.; Zhang, M.; Wu, Q.; Liu, M.; Jiang, L. Bio-inspired drag reduction: From nature organisms to artificial functional surfaces. *Giant* **2020**, *2*, 100017. https://doi.org/https://doi.org/10.1016/j.giant.2020.100017.
26. Evans, H.B.; Hamed, A.M.; Gorumlu, S.; Doosttalab, A.; Aksak, B.; Chamorro, L.P.; Castillo, L. Engineered bio-inspired coating for passive flow control. *Proceedings of the National Academy of Sciences* **2018**, *115*, 1210–1214, [https://www.pnas.org/doi/pdf/10.1073/pnas.171 https://doi.org/10.1073/pnas.1715567115.
27. Doosttalab, A.; Dharmarathne, S.; Bocanegra Evans, H.; Hamed, A.M.; Gorumlu, S.; Aksak, B.; Chamorro, L.P.; Tutkun, M.; Castillo, L. Flow modulation by a mushroom-like coating around the separation region of a wind-turbine airfoil section. *Journal of Renewable and Sustainable Energy* **2018**, *10*, 043305.
28. Santos, D.; Rogers, J.; De Rezende, A.; Maldonado, V. Exploring the Performance Boundaries of a Small Reconfigurable Multi-Mission UAV through Multidisciplinary Analysis. *Aerospace* **2023**, *10*. https://doi.org/10.3390/aerospace10080684.
29. Santos, D.; Ramirez, D.; Rogers, J.; Zamora, J.; Rezende, A.; Maldonado, V. Full-Cycle Design and Analysis of the Switchblade Reconfigurable Unmanned Aerial System. In Proceedings of the AIAA Aviation Forum; , 2022. https://doi.org/10.2514/6.2022-3207.
30. Maldonado, V.; Santos, D.; Wilt, M.; Ramirez, D.; Shoemaker, J.; Ayele, W.; Beeson, B.; Lisby, B.; Zamora, J.; Antu, C. 'Switchblade': Wide-Mission Performance Design of a Multi-Variant Unmanned Aerial System. In Proceedings of the AIAA Scitech 2021 Forum; 2021. https://doi.org/10.2514/6.2021-0213.
31. Vicroy, D.D.; Loeser, T.D.; Schütte, A. Static and Forced-Oscillation Tests of a Generic Unmanned Combat Air Vehicle. *Journal of Aircraft* **2012**, *49*, 1558–1583, [https://doi.org/10.2514/1.C031501]. https://doi.org/10.2514/1.C031501.
32. Marusic, I.; Monty, J.P.; Hultmark, M.; Smits, A.J. On the logarithmic region in wall turbulence. *Fluid Mechanics* **2013**, *716*, 389–420. https://doi.org/https://doi.org/10.1017/jfm.2012.511.
33. Österlund, J.M.; Johansson, A.V.; Nagib, H.M.; Hites, M.H. A note on the overlap region in turbulent boundary layers. *Physics of Fluids* **2000**, *12*, 1–4.
34. Maldonado, V.; Peralta, N.; Gorumlu, S.; Ayele, W. On the figure of merit and streamwise flow of a propulsive rotor with synthetic jets. *Aerospace Science and Technology* **2021**, *113*. https://doi.org/10.1016/j.ast.2021.106712.
35. Cook, M.J. *Flight Dynamics Principles: A Linear Systems Approach to Aircraft Stability and Control*, third edition ed.; Butterworth- Heinemann, 2013.

 doi:10.20944/preprints202410.1381.v1